Monte Carlo simulations of the XY vectorial Blume-Emery-Griffiths model in multilayer films for ^{3}He-^{4}He mixtures

J. B. Santos-Filho[1] and J. A. Plascak[2,3,4]

[1]*Instituto Federal de Ciências e Tecnologia de Sergipe 49100-000 São Cristóvão, Sergipe, Brazil*

[2]*Universidade Federal da Paraíba, Centro de Ciências Exatas e da Natureza-Campus I, Departamento de Física-CCEN Cidade Universitária 58051-970-João Pessoa, Paraíba-Brazil*

[3]*Departamento de Física-ICEx, Universidade Federal de Minas Gerais Caixa Postal 702, 30123-970 Belo Horizonte, Minas Gerais, Brazil*

[4]*Center for Simulational Physics, University of Georgia, Athens, Georgia 30602, USA*

(Received 21 June 2017; published 27 September 2017)

The XY vectorial generalization of the Blume-Emery-Griffiths (XY-VBEG) model, which is suitable to be applied to the study of ^{3}He-^{4}He mixtures, is treated on thin films structure and its thermodynamical properties are analyzed as a function of the film thickness. We employ extensive and up-to-date Monte Carlo simulations consisting of hybrid algorithms combining lattice-gas moves, Metropolis, Wolff, and super-relaxation procedures to overcome the critical slowing down and correlations among different spin configurations of the system. We also make use of single histogram techniques to get the behavior of the thermodynamical quantities close to the corresponding transition temperatures. Thin films of the XY-VBEG model present a quite rich phase diagram with Berezinskii-Kosterlitz-Thouless (BKT) transitions, BKT endpoints, and isolated critical points. As one varies the impurity concentrations along the layers, and in the limit of infinite film thickness, there is a coalescence of the BKT transition endpoint and the isolated critical point into a single, unique tricritical point. In addition, when mimicking the behavior of thin films of ^{3}He-^{4}He mixtures, one obtains that the concentration of ^{3}He atoms decreases from the outer layers to the inner layers of the film, meaning that the superfluid particles tend to locate in the bulk of the system.

DOI: 10.1103/PhysRevE.96.032141

I. INTRODUCTION

The general progress in the production and characterization techniques of thin film materials have enabled a deeper understanding of the physics of two-dimensional systems. In addition, it is now well known that the physical properties of monolayer films can, in some cases, drastically differ from their bulk three-dimensional (3D) counterpart. As a matter of example, the molybdenite [1], phosphorene [2], and silicene [3] present nowadays a high potential for electronic industry devices. On the other hand, superfluid helium in thin films also have distinct characteristics of their 3D bulk geometry and, as a consequence, these new features have led to a better understanding of rich phenomena such as Casimir effect [4,5], turbulence in superfluids [6], and phase transitions [7–9], among others.

In particular, the critical phase transitions in 3D superfluid ^{4}He permit an experimental study with unprecedented high resolution and with no complexities arising from impurities and crystalline imperfections [10–12]. In lower dimensions, the ^{4}He monolayer film shows a Berezinskii-Kosterlitz-Thouless (BKT) phase transition, which is different from the 3D bulk behavior, where the phase transition is always of second order. This characteristic of the films arises because of the translational symmetry breaking in one of the spatial direction.

On the other hand, computational studies by Schultka and Manousaki [13,14] have shown that multilayer films for the XY model (which belongs to the same universality class as ^{4}He), although exhibiting BKT transition, presents a superfluid density that varies along the layers, becoming stronger on the inner layers. This effect can be ascribed to the free boundary condition on the surfaces of the film.

The effect of boundary conditions have also been experimentally investigated in thin films of ^{3}He-^{4}He mixtures in different substrates [15–18]. In these mixtures, the ^{3}He atoms act as impurities, which reduce the superfluid transition temperature and drives the system toward a phase separation [19,20].

On the theoretical point of view, in 1971, Blume, Emery, and Griffiths [21] proposed a simple discrete spin model that could mimic the basic features of the bulk phase diagram of ^{3}He-^{4}He mixtures [22,23]. The model was first solved in the mean-field approximation and, for reasonable values of the parameters, it was able to qualitatively reproduce the experimental phase diagram of the ^{3}He-^{4}He mixture, including the tricritical point. The so-called Blume-Emery-Griffiths model (BEG) still continues being applied to treat several problems in condensed matter physics (see, for instance, Refs. [24,25] and references therein).

Despite the success in representing the physical realization of the ^{3}He-^{4}He mixtures in three dimensions, the BEG model presents a second-order phase transition in two-dimensional films, inconsistent with the experimental result of a BKT-like phase transition. This disagreement is related to the fact that the BEG model does not consider the rotational symmetry of the superfluid order parameter (the wave function of superfluid helium). Berker and Nelson [26], and independently Cardy and Scalapino [27], proposed a planar rotator model to account for the behavior of films of ^{3}He-^{4}He mixtures, known as the vector Blume-Emery-Griffiths model (VBEG). The phase diagram of the model was then investigated in two dimensions by using the Migdal-Kadanoff recursion relations and no tricritical point was found for any values of the Hamiltonian parameters. However, for the three-dimensional planar-rotator VBEG model, mean-field approximation and Monte Carlo simulations show critical endpoints, isolated critical or tricritical points, depending on the values of the

parameters [28]. Similar results to the plane-rotator model have also been obtained in the XY version of the VBEG model in three dimensions by using extensive Monte Carlo simulations [23] (the great advantage, in this latter model, is the presence of a true dynamics of the spins). Nevertheless, up to our knowledge, no results have been reported in the literature about the important properties of the XY-VBEG model on thin film structures, mainly regarding the topological BKT phase-transition as a function of film thickness, as well as the concentration of impurities on different layers of the thin film.

Thus, our purpose here is exactly to study ^{3}He-^{4}He mixtures on multilayer films using the XY-VBEG model, which presents three-dimensional spins. We will employ Monte Carlo simulations, combined with single histogram techniques, to examine the transition behavior as one gets from the two-dimensional system to the three-dimensional limit. This study on thin films will help us understand how the Berezinskii-Kosterlitz-Thouless endpoint and the isolated critical point, on two-dimensional lattices, tend to coalesce to a single tricritical point in the three-dimensional system. We can also address the important question of how the concentration of impurities varies along the layers of the film.

The scope of the paper is as follows. The model is defined in Sec. II. Section III is devoted to some details of the simulational methods, and the main results are presented in Sec. IV. The conclusions are briefly discussed in the last section.

II. MODEL AND THIN FILM STRUCTURE OF THE LATTICE

The XY vectorial generalization of the Blume-Emery-Griffiths model can be defined by the following Hamiltonian:

$$\mathcal{H} = -J \sum_{\langle ij \rangle} \left(S_i^x S_j^x + S_i^y S_j^y \right) - K \sum_{\langle ij \rangle} \vec{S}_i^2 \vec{S}_j^2 + \Delta \sum_{i=1}^{N} \vec{S}_i^2, \qquad (1)$$

where $\vec{S}_i$ represents a three-dimensional classical spin with components $\vec{S}_i = (S_i^x, S_i^y, S_i^z)$, and $\langle i, j \rangle$ means that the sums are taken only over nearest-neighbor pairs i, j on a thin film lattice of N sites. It is the first part of the above Hamiltonian that gives us the XY interaction (with exchange J) and mimics the superfluidity, as soon as one has an ordered spin state in the xy plane. On the other hand, this XY model can be viewed as embedded in a lattice-gas model, if we consider that the magnitude of the spin can take values $\vec{S}_i^2 = (S_i^x)^2 + (S_i^y)^2 + (S_i^z)^2 = 1$ or 0. This accounts for the existence of two different types of particles in the system: magnetic particles with $\vec{S}_i^2 = 1$ (^{4}He atoms), whose interactions play the role of the superfluid degrees of freedom, and nonmagnetic particles, with $\vec{S}_i^2 = 0$ (^{3}He atoms). Thus, the second term in the Hamiltonian arises from a phenomenological modeling of the interaction energy between pairs of helium particles of the same or different species. The parameter Δ, also known as the crystal field constant, is essentially the chemical potential difference $\mu_3 - \mu_4$ of ^{3}He and ^{4}He, respectively. In fact, this crystal field controls the density of impurities, which, in the present model, corresponds to the concentration of ^{3}He atoms. More details about the model can be found in reference [23]. As a matter of visualization, Fig. 1 depicts an example of a configuration of the model Eq. (1) on a cubic lattice with linear size $L = 30$.

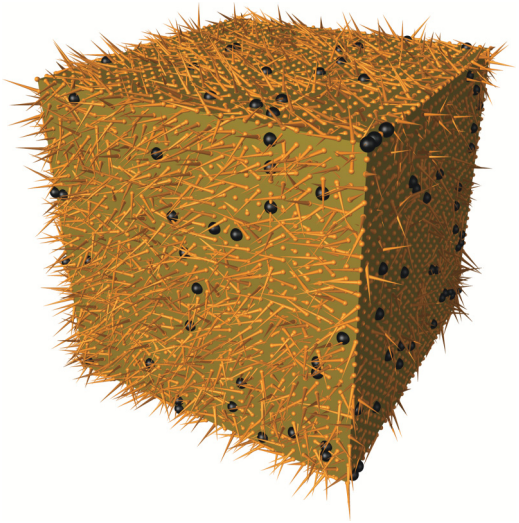

FIG. 1. Example of a configuration of the model described by Eq. (1) in a cubic lattice of size $L = 30$. The pins are the spin vectors representing ^{4}He atoms and the small black spheres represent the ^{3}He atoms. The concentration of ^{3}He (or similarly ^{4}He) atoms depends on the value of the crystal field Δ.

We consider here $J = K = 1$ and the reduced crystal field variable $d = \Delta/J$. These parameters correspond to the same typical values considered in different papers studying the system on a cubic lattice, both for the XY version as well as for the planar-rotator version of the model [29,30].

In this work, however, instead of treating a 3D lattice, we are going to consider the model on thin films of different thickness. A typical simulated film is outlined in Fig. 2. It is composed of a square lattice of size $L \times L$ with periodic boundary conditions in the x and y directions, and free boundary conditions in the z direction with thickness given by h. These boundary conditions have been chosen because the study of helium films on different substrates shows that the superfluid order parameter vanishes on the boundary of the film [31]. The free boundary condition can be interpreted as a Dirichlet boundary condition to the value of zero field on the surfaces [32]. An alternative choice of free boundary conditions is the staggered boundary condition. Numerical

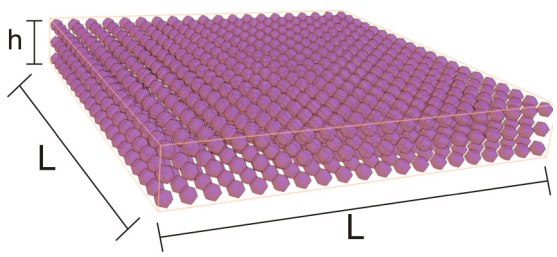

FIG. 2. Schematic drawing of a simulated multilayer film where the dots are the lattice sites. In the x-y plane we have an $L \times L$ square lattice (with $L = 20$ in this figure) with periodic boundary conditions in both directions, and free boundary conditions in the z direction with thickness given by h ($h = 3$ in this example).

results in other types of models have shown, however, that free and staggered boundary conditions have the same results for the corresponding universal quantities [33].

III. SIMULATIONAL METHODS

To get the thermodynamic quantities and the corresponding phase diagram of the present model, we have used analytical and Monte Carlo simulation techniques. In the simulations, we have employed algorithms such as lattice-gas moves combined with spin-reorientation updates.

The lattice-gas moves account for the phase separation in the model. The lattice-gas update attempts to insert a magnetic particle with a randomly selected spin orientation at a site where a nonmagnetic one is located, or to replace the magnetic particle present at a site by a nonmagnetic one. The acceptance probability is set by the local heat-bath rule

$$p(\Delta E) = 1/[\exp(\Delta E/k_B T) + 1], \tag{2}$$

where ΔE is the change in configurational energy of the proposed move, k_B is the Boltzmann constant (set to unity in the present work), and T is the temperature of the system. The single spin-reorientation update is done as in the Metropolis algorithm, but the acceptance probability is also given by the local heat-bath rule given by Eq. (2).

The spin reorientation updates are related to the long-range magnetic order, which corresponds to the superfluid phase. We also applied nonergodic versions of the Wolff algorithm [34,35] and overrelaxation updates of the spins at constant configurational energy [36,37]. Each update method is performed in sweeps over the full lattice and each method is preceded by a lattice-gas sweep. Thus, the Monte Carlo update algorithms, each one preceded by the lattice-gas update, are all combined resulting in a hybrid Monte Carlo method to reduce correlations between successive configurations in the simulation.

The Wolff update affects only the in-plane components of the spin-1 particles, while the z component is unchanged to obey detailed balance. Analogously, the overrelaxation method is performed with a rotation solely of the in-plane component of the spins to keep the configurational energy fixed. Although the Wolff and the overrelaxation updates are both nonergodic, with the spin-reorientation updates and the lattice gas moves included, the combined algorithm will satisfy the ergodicity condition. This comes from the fact that for each lattice-gas or spin reorientation moves, the new spin direction is randomly selected from the even distribution on a unit sphere. Thus, what we will henceforth call a hybrid Monte Carlo step (MCS) is defined by one spin-reorientation sweep, one Wolff cluster update, and one overrelaxation sweep. Of course, different combinations of these algorithms can also be chosen, but this choice has been proven to be efficient in terms of reducing the correlations and time consuming.

Simulations have been done on lattices with dimensions $L \times L \times h$, with periodic boundary conditions perpendicular to the direction of the film thickness and free boundary conditions in the direction of the thickness h. The runs comprised 5×10^3 MCS for equilibration and the preliminary measurements were made on 10^5 hybrid MCS for each lattice. The lattice sizes ranged from $L = 16$ to $L = 128$, and the thickness $h = 1, 2, 3,...$ up to 11 (in some special cases we also considered $h = 20$). When needed, additional lattices with sizes $L = 256$ and $L = 512$ have also been simulated. The routine RAN2 [38] was the random number generator used in all simulations.

The global phase diagram, as a function of the theoretical parameters, has been obtained through the location of the BKT transition temperature by analyzing the behavior of the magnetic susceptibility, as well as the helicity modulus. At some special points of the phase diagram, which needed a better accuracy, we have employed the single histogram technique [39]. For these special points, the system has been again simulated with 5×10^3 MCS for equilibration and now 5×10^6 hybrid MCS for getting the single histogram calculations.

It has been noticed that the absence of well-defined peaks in the thermodynamic quantities makes a precise location of the BKT transition temperature more difficult in this model. Therefore, different approaches have been carried out to estimate the BKT transition point and verify which one best fits the analysis of the XY-VBEG model. Several quantities have been studied to obtain the complete phase transition diagram, as well as to check if the whole characteristics of BKT transitions are preserved at all points of the diagram for films of different thickness h.

Although model Eq. (1) does not present a finite magnetization in the absence of an external magnetic field in two dimensions, it does present (in the thermodynamic limit) a phase transition in which the in-plane susceptibility diverges exponentially as the Berezinskii-Kosterlitz-Thouless temperature ($T_{\rm BKT}$) is approached from above and stays infinite for $T \leqslant T_{\rm BKT}$ in such a way that an entire line of critical points appears in the phase diagram [40].

On the other hand, for finite systems of linear size L and $h = 1$, the above susceptibility for $T \leqslant T_{\rm BKT}$ is finite, but should behave as

$$\chi \propto L^{2-\eta}, \tag{3}$$

where $\eta = \eta(T)$ is the corresponding correlation function exponent which depends on temperature. It is known that at the BKT transition temperature the exponent η has an established value of $\eta(T_{\rm BKT}) = 1/4$ [41] for pure and diluted systems [42,43]. This equation is, in general, used to estimate the BKT transition temperature [42–45]. We will assume here that a similar behavior can also be valid for lattices where the thickness h is different from $h = 1$.

IV. RESULTS

As has been discussed above, we have considered herein the case where $K = J = 1$, since these values of parameters have already been considered in the study of the three-dimensional version of the model Eq. (1) and a comparison can be achieved by just analyzing the results in the limit of very large thickness h.

A. Transition temperatures and phase diagrams

We have first computed the in-plane-magnetization susceptibility by averaging the square in-plane magnetization [40],

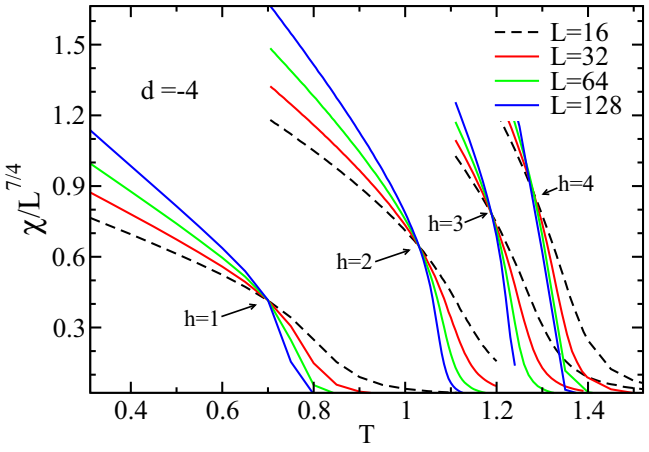

FIG. 3. Rescaled magnetic susceptibility as a function of the temperature for different lattice sizes L and thicknesses h. In this case $d = -4$. For a question of clarity, the Monte Carlo data have been omitted and only the lines are shown in this figure.

$$\chi = \chi_{xy} = \langle m_{xy}^2 \rangle, \tag{4}$$

where

$$m_{xy}^2 = \frac{1}{N} \sum_{i=1}^{N} \left[\left(S_i^x\right)^2 + \left(S_i^y\right)^2 \right], \tag{5}$$

and $N = L \times L \times h$ is the number of lattice sites.

In Fig. 3 it is shown the behavior of $\chi / L^{2-\eta}$ as a function of temperature for lattice sizes ranging from $L = 16$ to $L = 128$, and thicknesses $h = 1,2,3,4$, for $d = -4$, with the value of the critical exponent $\eta = 1/4$ at the BKT transition. The temperature T here is measured in units of the Boltzmann constant. This value of the crystal field has been chosen because it gives a good quantitative view of the results. Note that for negative values of d one has a higher concentration of ^{4}He atoms, the concentration being 100% only in the limit $d \to -\infty$. On the other hand, for positive values of d, a higher presence of ^{3}He atoms is expected and, as we shall see below, a first-order transition will take place for some high enough ^{3}He concentration. Eventually, even the first-order transition will disappear when the crystal field continues to increase.

The intersections of curves for different lattice sizes, as depicted in Fig. 3, can give a good estimate for the BKT transition temperature. We can observe that the qualitative behavior of the curves for different thicknesses h is very similar, i.e., the curves for different values of L intersect at a single point, with the intersection temperatures increasing as the value of the film thickness h increases (as expected, since more interactions are introduced into the system). The temperatures so obtained are shown in Table I. For the monolayer film $h = 1$ the BKT transition temperature $T_{\rm BKT}^{\chi} = 0.6975(14)$ is slightly smaller than the corresponding one for the two-dimensional XY model $T_{\rm BKT} = 0.700(5)$ [46].

Another thermodynamic quantity that has been investigated is the helicity modulus Υ, also known as stiffness, which is a thermodynamic quantity often employed in the XY model study. It was introduced by Cuccoli [40] to define the coherence

TABLE I. BKT transition temperature obtained by the scaling law susceptibility ($T_{\rm BKT}^{\chi}$) and the helicity modulus ($T_{\rm BKT}^{\Upsilon}$) in different film thicknesses for $K = J = 1$ and $d = -4$.

h	$T_{\rm BKT}^{\chi}$	$T_{\rm BKT}^{\Upsilon}$
1	0.6975(14)	0.700(1)
2	1.0305(5)	1.030(3)
3	1.1895(20)	1.189(5)
4	1.281(1)	1.282(8)

length of a ^{4}He superfluid, which corresponds to superfluid density on the XY model formalism. Υ describes then the resistance of the system to a turning of the planar spin components at a certain direction. The helicity modulus can be expressed as

$$\Upsilon = \left. \frac{\partial^2 F}{\partial \delta^2} \right|_{\delta=0}, \tag{6}$$

where $F = -k_B T \ln(Z)$ is the free energy of the system, Z its canonical partition function, and δ a phase twist applied to the boundaries along the x direction. Developing Eq. (6), one is able to arrive at a general expression given by [47]

$$\Upsilon = \left\langle \left. \frac{\partial^2 \mathcal{H}}{\partial \delta^2} \right|_{\delta=0} \right\rangle - \frac{1}{k_B T} \left\langle \left(\left. \frac{\partial \mathcal{H}}{\partial \delta} \right|_{\delta=0} \right)^2 \right\rangle - \frac{1}{k_B T} \left\langle \left. \frac{\partial \mathcal{H}}{\partial \delta} \right|_{\delta=0} \right\rangle^2, \tag{7}$$

where $\mathcal{H}$ is the Hamiltonian of the system. For the particular XY-VBEG model, Eq. (1), one has

$$\left. \frac{\partial H}{\partial \delta} \right|_{\delta=0} = -J \sum_{i \neq j} (\vec{r}_{ij} \cdot \hat{x}) \left(S_i^x S_j^y - S_i^y S_j^x \right), \tag{8}$$

$$\left. \frac{\partial^2 H}{\partial \delta^2} \right|_{\delta=0} = J \sum_{i \neq j} (\vec{r}_{ij} \cdot \hat{x})^2 \left(S_i^x S_j^x + S_i^y S_j^y \right), \tag{9}$$

where $\vec{r}_{ij}$ is the vector distance of the spin $\vec{S}_i$ to spin $\vec{S}_j$ and $\hat{x}$ is the unit vector along the x direction.

In the thermodynamic limit, the helicity modulus presents a jump from $2T/\pi$ to 0 at the BKT transition temperature for a monolayer system [41]. So, the helicity modulus can also be used to estimate the BKT transition temperature [48–50]. Although this behavior has been obtained for unalloyed case, its extension to the diluted system has shown to be still valid [43]. In addition, arguments from self-consistent harmonic approximation (SCHA) have shown that the helicity module at $(2T_{\rm BKT}/\pi)$ should be independent of the impurities concentration (see, for instance, Ref. [51]). On the other hand, in multilayer films the helicity module shows a jump of $2T/\pi h$ at the corresponding BKT transition temperature [13,14], with h being the number of film layers.

In Fig. 4 we have the helicity modulus as a function of temperature of the XY-VBEG model for different (larger) lattice sizes L and the same thicknesses h as before, for $d = -4$. It was obtained from Monte Carlo simulations using Eqs. (7), (8), and (9). We have estimated the transition temperature from the crossings of the helicity modulus with

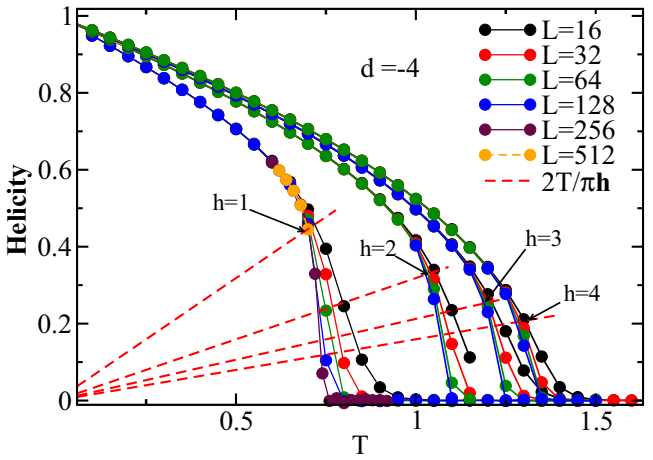

FIG. 4. Helicity modulus curve as a function of temperature of the XY-VBEG model for different lattice sizes L and thickness h. The full circles are simulation results, and the lines are guide to the eyes. The dashed lines correspond to the linear equation $2T/\pi h$. The error bars are smaller than the symbol sizes.

the straight line $2T/\pi h$, as shown in Fig. 4. The temperatures so obtained are also shown in Table I. In this table, one can observe that the temperature obtained from the susceptibility scaling law is comparable to that from the helicity modulus, however, the former one has a better precision. Therefore, the BKT transition line of the phase diagram for other values of the reduced crystal field d, as well as thickness of the films h, has been determined utilizing the susceptibility scaling law (3). Note also that the transition temperature for the monolayer system, namely $T_{\rm BKT}^{\Upsilon} = 0.700(1)$, is in this case also comparable to the pure XY model transition temperature $T_{\rm BKT} = 0.700(5)$ [46], which means that at $d = -4$ one practically has the ^{4}He superfluid system.

To see the behavior of the transition temperature as a function of the thickness of the film, in Fig. 5 we have the BKT

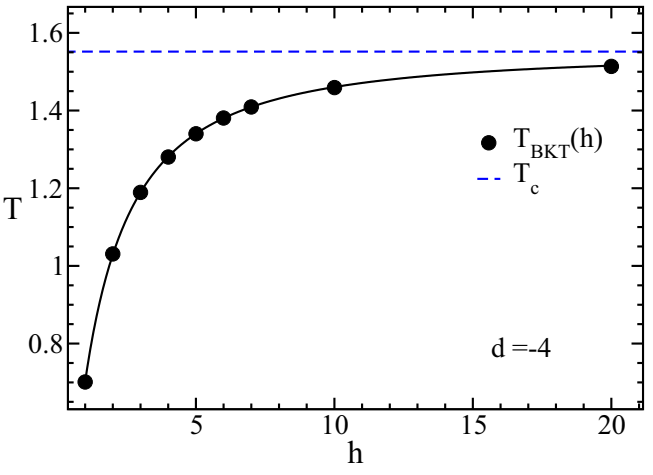

FIG. 5. BKT transition temperature as a function of film thickness h for $d = -4$. The full line is a fit to Eq. (10). The horizontal dashed line marks the transition temperature of the corresponding three-dimensional system.

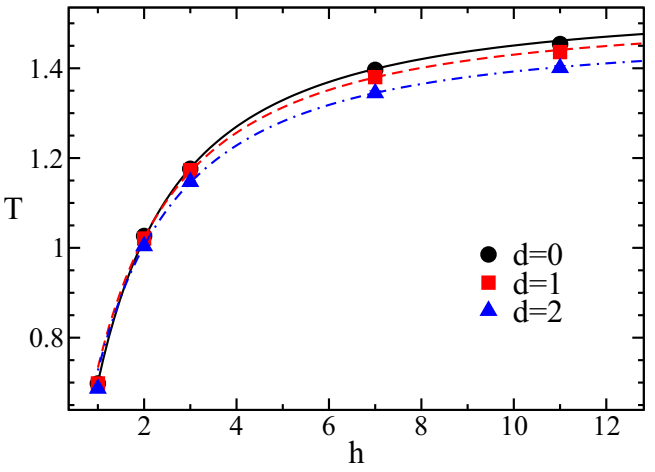

FIG. 6. BKT transition temperature as a function of film thickness h for different values of crystal field d. The lines are fits to Eq. (10).

transition temperature as a function of h for $d = -4$, together with the critical temperature for the corresponding 3D lattice, which is clearly approached when $h \to \infty$. Figure 6 shows the BKT transition temperature as a function of the thickness h for other values of crystal field. It can be noticed a similar behavior for different values of h. However, as expected, the transition temperature decreases as one increases the value of d. This is so because as one increases the crystal field one also increases the concentration of nonmagnetic particles, implying a decrease of the corresponding transition temperature.

As has been reported by Schultka and Manousakis [13,14], the BKT transition temperature of the XY model defined on thin films follows a scaling relation with the film thickness h. For the particular case of the planar rotator model, this scaling relation is given by

$$T_{\rm BKT}(h) = T_c^{3d}\left[1 + \frac{a}{(h+b)^{1/\nu}}\right], \qquad (10)$$

where a and b are nonuniversal constants, ν and T_c^{3d} are the critical exponent and the critical temperature of the three-dimensional system, respectively. It is interesting to notice that the above equation also fits very well the results of the present more general XY-VBEG model. In fact, the full line in Fig. 5 has been obtained by using the known parameters of Eq. (10), that is, the exponent of the three-dimensional system $\nu = 0.6717(1)$ [52] and the critical temperature of the three-dimensional system $T_c^{3d} = 1.5518(2)$. Adjusting the respective constants one obtains $a = 1.587(8)$ and $b = -2.25(1)$. In Fig. 6 it is shown the same fit for other crystalline field values where different values for a and b have been obtained. The corresponding temperature of the three-dimensional system has been taken from Freire *et al.* [23]. From the quality of the fits one can clearly see that Eq. (10) can also account for the behavior of the transition temperature as a function of the film thickness for the present more general XY-VBEG model.

To have a better picture of the phase transition properties of the present model as we change the thickness h, we have also computed the constant volume specific heat c_v, which is given

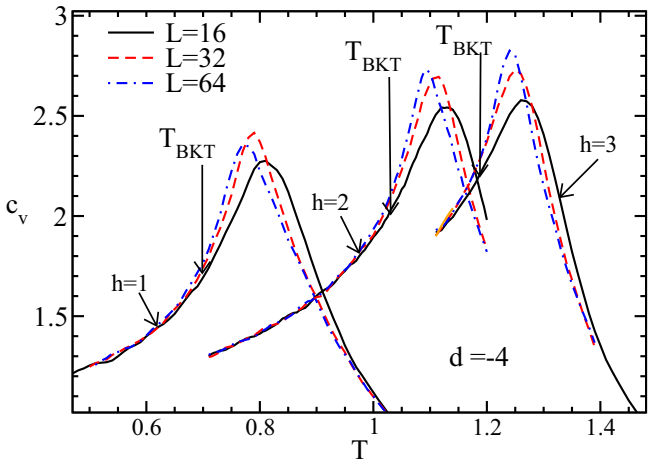

FIG. 7. Specific heat c_v as a function of the temperature for different lattice sizes L and thicknesses h for $d = -4$. The longer vertical arrows indicate the BKT transition. As in Fig. 3, the Monte Carlo data have been omitted for clarity.

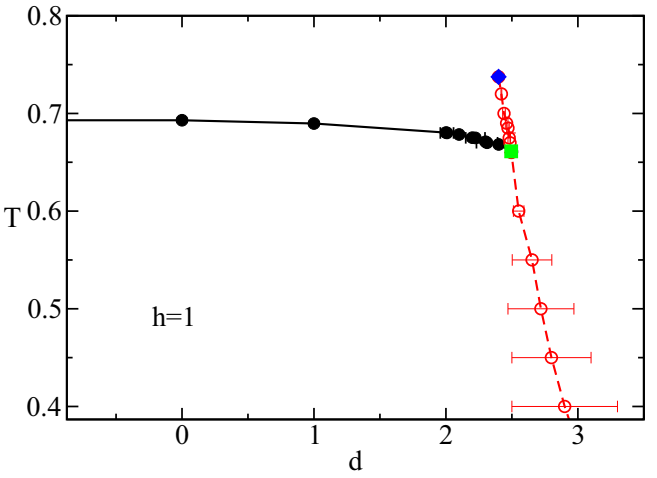

FIG. 8. Phase diagram in the temperature versus reduced crystal field plane for $J = K = 1$ and $h = 1$. The full circles indicate BKT transitions and open circles first-order transitions. The full square and diamond represent the BKT transition endpoint and the isolated critical point, respectively. The lines are guide to the eyes.

by

$$c_v = N\frac{\langle E^2\rangle - \langle E^2\rangle^2}{T^2}, \tag{11}$$

where E is the energy per spin and T is the temperature of the system. Figure 7 shows the specific heat as a function of temperature for the crystal field $d = -4$, for three different lattice sizes, and thicknesses $h = 1$, 2, and 3. As can be seen, the specific heat has a maximum at a temperature higher than the transition temperature $T_{\rm BKT}$ with no detectable singularity. As in the monolayer lattice ($h = 1$), this maximum is caused by the gradual dissociation of vortex pairs [26] and there is no clear correlation between the simulated lattice size L and the corresponding height of the maximum for small values of h. However, for $h \geqslant 3$, we have observed that a correlation between L and the maximum specific heat for these lattice sizes starts taking place, in such a way that as the lattice increases, the peak also systematically increases (as for $h = 3$ shown in Fig. 7). In addition, the temperature at which the maximum of specific heat happens is approaching the BKT transition temperature with the increase of h. As a matter of example, the difference between the temperature of the maximum of the specific heat peak and the BKT transition temperature for $L = 64$ and $h = 1$ is 0.073(2), for $h = 2$ is 0.059(1), and for $h = 3$ is 0.053(1). As a result, the film exhibits indeed a BKT-type transition, but with some features that are similar to a second-order transition at higher temperatures (just *similar*, because there is a kind of crossover from one behavior to the other and the true second-order transition will only be achieved in the limit $h \to \infty$). Although such specific heat behavior can be seen for larger values of h, there is not a second-order finite size scaling for it and, from the present simulations, we cannot provide a more detailed discussion on the underlying physical mechanisms leading the unconventional BKT phase transition to become a conventional continuous one.

Thus, the global phase diagram, for a given finite value of the film thickness, can be obtained through the location of the BKT transition by analyzing the behavior of the magnetic susceptibility, as given by Eq. (4). However, as we change the crystal field, possible first-order transitions can be set up in the model, and multicritical points will also be present depending on how the second-order line meets the first-order line. To seek for first-order transitions we have analyzed the hysteresis observed in the susceptibility χ_{xy} and also in the concentration q of ^{3}He (nonmagnetic) particles. The ^{3}He concentration q can be easily obtained from

$$q = \frac{1}{L^2}\sum_i^N \left[1 - \langle S_i^2\rangle\right]. \tag{12}$$

It turns out q to be an order parameter that allows us to identify first-order transitions present in the studied system. Although through this approach the location of the first-order transition line is not as precise as the corresponding second-order transition line, it is sufficient to determine the full phase diagram for a given value of the film thickness as a function of the crystal field, mainly close to the multicritical points. As an example, Fig. 8 depicts the result for the special case of a monolayer film ($h = 1$), where we can clearly see the presence of a BKT transition endpoint and an isolated critical point. This is the same feature that was obtained for the triangular lattice [29].

The corresponding phase diagrams, in the crystal field versus temperature plane, of the XY-VBEG model for $K = J = 1$ and different thicknesses are shown in Fig. 9. Although the three-dimensional model has a second-order transition line and a tricritical point, for any finite value of the thickness h one has a BKT transition line, a BKT endpoint and an isolated critical point. The BKT endpoint and the isolated critical point get close together as the film thickness increases and eventually coalesce into the tricritical point in the $h \to \infty$ limit. Figure 10 shows such behavior in the temperature versus crystal field plane.

Regarding the three-dimensional model, the concentration of nonmagnetic particles at the tricritical point $q_{\rm TCP}$, and the

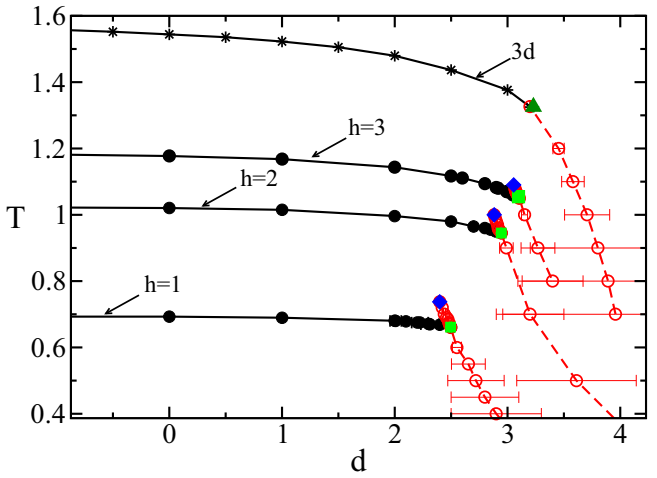

FIG. 9. Phase diagrams in the temperature versus reduced crystal field plane for $J = K = 1$ and films with different thicknesses h. The data for the three-dimensional model have been taken from Ref. [23]. The full circles indicate BKT transitions, the stars second-order phase transitions, and open circles first-order transitions. The full squares, diamonds, and the triangle represent BKT transition endpoints, isolated critical points, and the tricritical point, respectively. The lines are guide to the eyes.

ratio $T_{\rm TCP}/T_c^0$, where $T_{\rm TCP}$ is the tricritical temperature and $T_c^0 = T_c^{3d}$ is the temperature of the superfluid transition for pure ^{4}He, are two parameters that can be used to compare the theoretical results with the experimental data (see, for instance, Ref. [23] for the three-dimensional model). Similarly, in this work we can study equivalent quantities (although we are not aware yet of such experimental results), which are the concentration of ^{3}He at the BKT transition endpoint ($q_{\rm BKTEP}$) and the ratios $T_{\rm BKTEP}(h)/T^0_{\rm BKT}(h)$ and $T_{\rm CP}(h)/T^0_{\rm BKT}(h)$ to verify how the new free boundary conditions influence the behavior of these parameters. In the above relations, $T_{\rm BKTEP}(h)$ is the temperature of the BKT endpoint, $T^0_{\rm BKT}(h)$ the temperature of the BKT transition of the pure system, and $T_{\rm CP}(h)$ is the

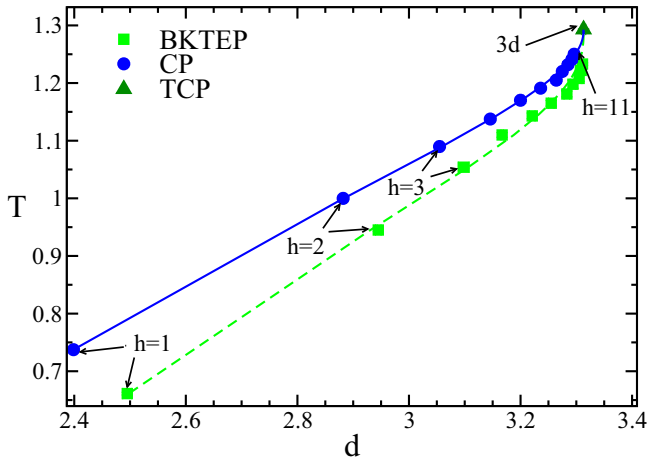

FIG. 10. Isolated critical points (CP) and BKT transition endpoints (BKTEP) coalescing into the tricritical point (TCP) as the film thickness increases. The lines are just guide to the eyes.

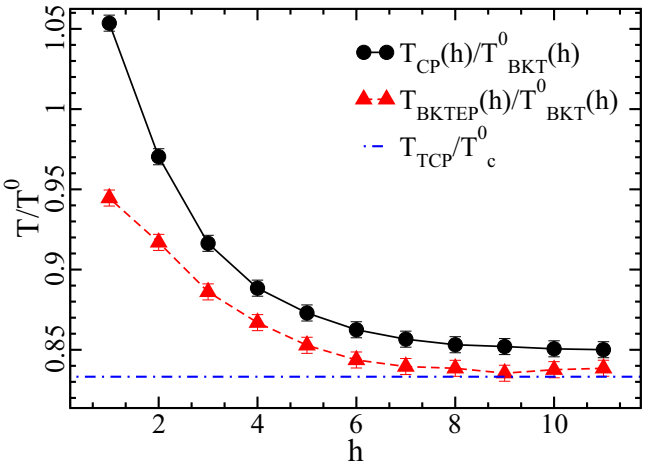

FIG. 11. Ratios $T_{\rm CP}(h)/T^0_{\rm BKT}(h)$ and $T_{\rm BKTEP}(h)/T^0_{\rm BKT}(h)$ of the XY-VBEG model with $K = J = 1$ for different thicknesses h. The lines are guide to the eyes. The ratio $T_{\rm TCP}/T_c^0$ of the three-dimensional model [23] is represented by the dot-dashed line.

temperature of the isolated critical point, all quantities as a function of the film thickness h. Figure 11 shows the ratios $T_{\rm BKTEP}(h)/T^0_{\rm BKT}(h)$ and $T_{\rm CP}(h)/T^0_{\rm BKT}(h)$ obtained in this work and $T_{\rm TCP}/T_c^0$ for the three-dimensional system taken from Ref. [23]. It is noted that the ratios $T_{\rm BKTEP}(h)/T^0_{\rm BKT}(h)$ and $T_{\rm CP}(h)/T^0_{\rm BKT}(h)$ rapidly approach $T_{\rm TCP}/T_c^0$ with the increasing of film thickness.

B. Layer distribution of ^{3}He particles

It is interesting now to analyze the behavior of the distribution of ^{3}He particles q as a function of h. Figure 12 shows the mean concentration of ^{3}He particles at the BKT critical endpoint for films of different thicknesses. It is quite interesting to notice that there is no convergence to the tricritical point value of the three-dimensional model in this case, as should be expected. For film thickness $h = 11$, for example, at the

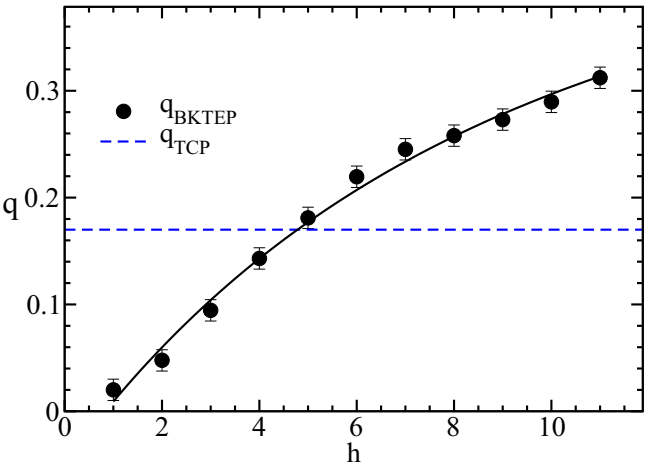

FIG. 12. Average concentration of ^{3}He at the BKT endpoint as a function of thickness. Dots are results from simulations, the dashed horizontal line is the result for the three-dimensional model, and the solid line is just a guide to the eyes.

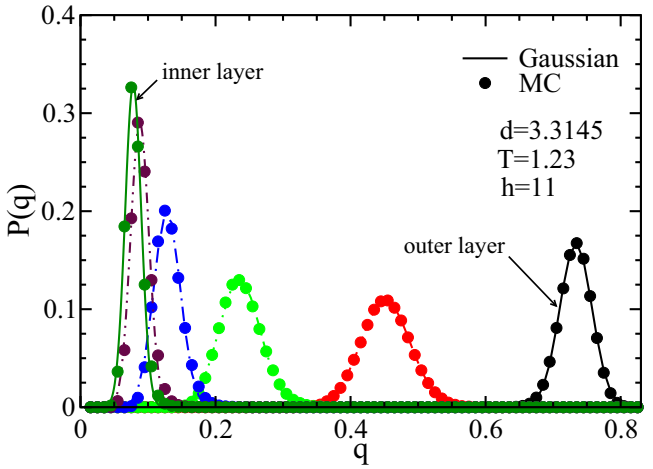

FIG. 13. Probability distribution of the nonmagnetic ^{3}He particles $P(q)$ at several layers of a thin film with thickness $h = 11$ and $L = 40$. The full circles are simulational results and the lines a Gaussian fit to the corresponding data.

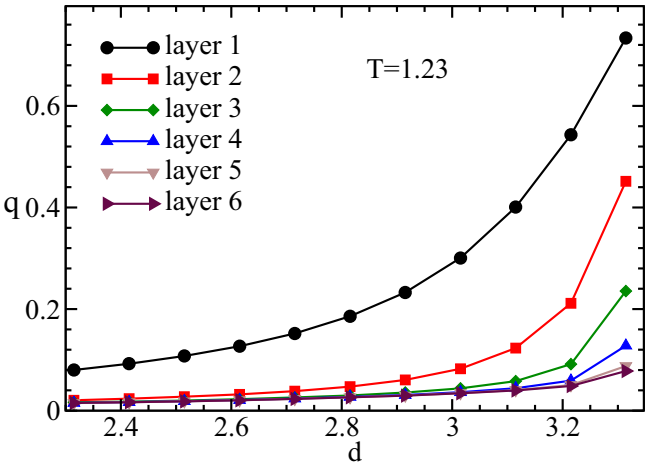

FIG. 14. Concentration of ^{3}He in each layer as a function of crystal field. Dots are results of the simulation and the lines are guides to the eye.

BKT transition endpoint one has $q_{\mathrm{BKTEP}} = 0.312$, almost twice the concentration of the three-dimensional model at the tricritical point, which is $q_{\mathrm{TCP}} = 0.17$ [23] (the ^{3}He concentration at the tricritical point of the three-dimensional system was experimentally measured as $q_{\mathrm{TCP}} = 0.67$ [20]). This anomalous growth of q with the thickness indicates that higher concentrations of non-magnetic particles can be achieved as a result of the free boundaries present on the thin films.

A better way to track what is happening with the distribution of the nonmagnetic particles, due to the presence of the free surfaces, is to compute their concentrations on each layer of the film, instead of the total mean concentration as depicted in Fig. 12. Of course, layers with the same distance from the free surfaces will have the same concentrations, owing to the symmetry of the lattice. As an example, let us see the results for a thin film of thickness $h = 11$ and linear size $L = 40$. Thus, the concentrations to be analyzed are provided only by the first six layers, where the first layer is the outermost one and the innermost one is the sixth layer of the film. Figure 13 shows the probability distribution of the concentration of ^{3}He that comes from the simulation results at the specific point $T = 1.23$ and $d = 3.3145$ for each one of the six layers. In this particular point the system is in the superfluid phase very close to the first-order transition line. The figure also shows a Gaussian fit to the data, from which one can easily calculate the average and variance of the nonmagnetic concentration. One can see that the average concentration of ^{3}He decreases from the outer layer (layer one) to the inner layer (layer six) and the superfluid particles tend to locate in the bulk of the film (note that, for the outer layer, $\langle q \rangle = 0.73372(6)$ in this case). This means that, for very large values of the thickness h, the bulk of the film behaves as a three-dimensional system, with its proper concentration of ^{3}He . However, due to the presence of the free surfaces at the edges of the film, the concentration of ^{3}He tends to increase in layers close to the surface. In this way, the total concentration of ^{3}He particles in the film will surely be greater than the corresponding concentration for the three-dimensional infinite lattice. This explains in some way the results depicted in Fig. 12.

In Fig. 14 it is shown the average concentration of the nonmagnetic particles as a function of the reduced crystal field d for the six layers with $h = 11$ at the temperature $t = 1.23$. It is also observed that the increase of q with the crystal field is more sensitive at the outer layers.

Finally, in Figs. 15(a)–15(d) we show the concentration distribution of ^{3}He at the first-order transition point $T = 1.23$ and $d = 3.315$. It can be seen that, as expected, the distribution has now two peaks for each layer. In the first layer the peaks have different heights and as one goes to the inner layers, the corresponding two peaks get more separated and tend to have the same height.

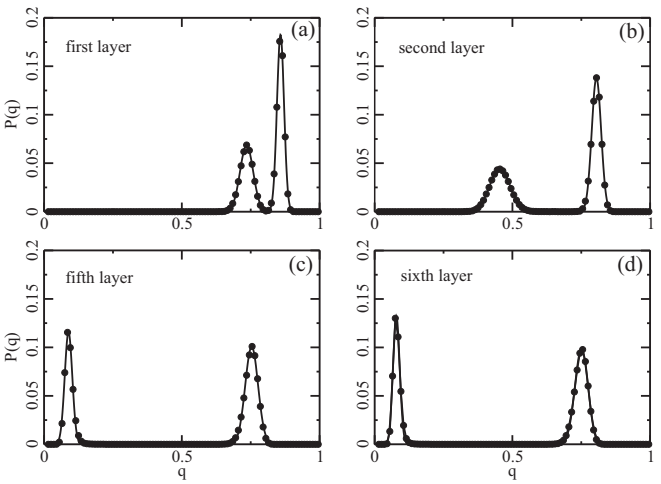

FIG. 15. Probability distribution of nonmagnetic particles in different layers at a point on the line of first-order transition. Dots are simulation results and the dashed lines are Gaussian fits. (a) First layer, (b) second layer, (c) fifth layer, and (d) sixth layer.

V. CONCLUDING REMARKS

In this paper, we have studied the XY-VBEG model in thin films using Monte Carlo simulations and histogram techniques. This model has an experimental appeal because it is suitable to describe ^{3}He-^{4}He mixtures. The multilayer films of this model showed a phase transition of BKT type with the same characteristics of the corresponding monolayer film. The results have been obtained for the particular case $K = J = 1$, since for these values one can compare to the corresponding results obtained in the literature for the three-dimensional model.

Using a finite-size scaling relation of the in-plane magnetic susceptibility with exponent $\eta = 1/4$ for films of different thicknesses, we have obtained the BKT transition temperature that matches the BKT temperature obtained from the helicity modulus. Thus, one can say that the exponent $\eta = 1/4$ does not vary with film thickness and it can be used to obtain BKT transition lines for films of different thicknesses.

On the other hand, the BKT transition temperature increases with the film thickness and tends to the second-order transition temperature of the three-dimensional model when the film thickness goes to infinity. A good fit of the BKT transition temperature with the thickness of the film has been obtained by using the scaling relation proposed by Schultka and Manousakis for the planar rotator model. The same critical exponent ν of the three-dimensional model was used for different values of the crystal field, showing a same universality class in this case. It is noteworthy that previous works have showed that the critical exponents ν does not vary even with quenched dilution [53].

The phase diagram to thin films has a BKT critical endpoint and an single critical point. These points approach each other with the increasing of thickness and coalesce at the tricritical point of the three-dimensional system. However, due to the presence of the free surfaces, the concentration of non-magnetic particles at the tricritical point is twice the value of the bulk system for large values of h. It means that although the transition temperatures approach the three-dimensional value as $h \to \infty$, without being sensitive to the boundary conditions, the concentration of magnetic and nonmagnetic particles are quite different and strongly depends on the layer distance of the surface. This layer dependence of the concentration is mainly seen at the first-order transition lines.

The first-order phase transition lines have been located by analyzing the hysteresis observed in the susceptibility and in the ^{3}He concentration. However, from Fig. 15 one can clearly see that the double peak present on the q concentration can also be a good quantity to locate, in a more precise way, such first-order transitions. Note that no double peak structure is observed for $d = 3.3145$, while they are clear when $d = 3.315$. Nevertheless, we have not pursued this further in the present work because the multicritical points, and the general topology of the phase diagrams, will not significantly change by using this more sophisticated approach. It will, of course, be necessary for a more precise location of the BKT transition endpoints and the isolated critical points.

ACKNOWLEDGMENTS

We thank R. T. S. Freire for fruitful discussions and the help on some figures. Financial support from PROPEX-IFS CNPq, CAPES, and CNPq under Grant No. 402091/2012-4 is gratefully acknowledge.

[1] B. Radisavljevic, A. Radenovic, J. Brivio, V. Giacometti, and A. Kis, Nat. Nanotechnol. **6**, 147 (2011).
[2] H. Liu, A. T. Neal, Z. Zhu, Z. Luo, X. Xu, D. Tománek, and P. D. Ye, ACS Nano **8**, 4033 (2014).
[3] P. Vogt, P. DePadova, C. Quaresima, J. Avila, E. Frantzeskakis, M. C. Asensio, A. Resta, B. Ealet, and G. LeLay, Phys. Rev. Lett. **108**, 155501 (2012).
[4] J. B. S. Abraham, G. A. Williams, and K. Penanen, J. Low Temp. Phys: Conf. Ser. **568**, 012025 (2014).
[5] A. Maciołek and S. Dietrich, Europhys. Lett. **74**, 22 (2006).
[6] W. Guo, D. N. McKinsey, A. Marakov, K. J. Thompson, G. G. Ihas, and W. F. Vinen, J. Low Temp. Phys. **171**, 497 (2013).
[7] C. Zhang, K. Nho, and D. P. Landau, Phys. Rev. B **73**, 174508 (2006).
[8] R. Tiwari and W. I. Glaberson, Phys. Rev. B **42**, 2075 (1990).
[9] R. Ramos and O. Vilches, J. Low Temp. Phys. **134**, 55 (2004).
[10] J. A. Lipa, D. R. Swanson, J. A. Nissen, T. C. P. Chui, and U. E. Israelsson, Phys. Rev. Lett. **76**, 944 (1996).
[11] J. A. Lipa, D. R. Swanson, J. A. Nissen, Z. K. Geng, P. R. Williamson, D. A. Stricker, T. C. P. Chui, U. E. Israelsson, and M. Larson, Phys. Rev. Lett. **84**, 4894 (2000).
[12] J. A. Lipa, J. A. Nissen, D. A. Stricker, D. R. Swanson, and T. C. P. Chui, Phys. Rev. B **68**, 174518 (2003).
[13] N. Schultka and E. Manousakis, J. Low Temp. Phys. **109**, 733 (1997).
[14] N. Schultka and E. Manousakis, Phys. Rev. B **51**, 11712 (1995).
[15] T. Oda and M. Hieda, Phys. Rev. Lett. **111**, 106101 (2013).
[16] M. Morishita, J. Low Temp. Phys. **171**, 664 (2013).
[17] H. Yamaguchi, T. Oda, M. Hieda, T. Matsushita, and N. Wada, J. Low Temp. Phys. **171**, 650 (2013).
[18] M. Hieda, T. Oda, T. Matsushita, and N. Wada, J. Phys.: Conf. Ser. **400**, 012017 (2012).
[19] H. A. Kierstead, J. Low Temp. Phys. **35**, 25 (1979).
[20] E. H. Graf, D. M. Lee, and J. D. Reppy, Phys. Rev. Lett. **19**, 417 (1967).
[21] M. Blume, J. V. Emery, and R. B. Griffiths, Phys. Rev. A **4**, 1071 (1971).
[22] J. A. Plascak, A. M. Ferrenberg, and D. P. Landau, Phys. Rev. E **65**, 066702 (2002).
[23] R. T. S. Freire, S. J. Mitchell, J. A. Plascak, and D. P. Landau, Phys. Rev. E **72**, 056117 (2005).
[24] N. Farahmand Bafi, A. Maciolek, and S. Dietrich, Phys. Rev.E **91**, 022138 (2015).
[25] F. Antenucci, A. Crisanti, and L. Leuzzi, J. Stat. Phys. **155**, 909 (2014).
[26] A. N. Berker and D. R. Nelson, Phys. Rev. B **19**, 2488 (1979).
[27] J. L. Cardy and D. J. Scalapino, Phys. Rev. B **19**, 1428 (1979).

[28] A. Maciolek, M. Krech, and S. Dietrich, Phys. Rev. E **69**, 036117 (2004).
[29] J. B. Santos-Filho, J. A. Plascak, and D. P. Landau, Physica A **389**, 2934 (2010).
[30] B. S. Dillon, S. Chiesa, and R. T. Scalettar, Phys. Rev. B **82**, 184421 (2010).
[31] S. Mehta, M. O. Kimball, and F. M. Gasparini, J. Low Temp. Phys. **114**, 467 (1999).
[32] M. Hasenbusch, J. Stat. Mech.: Theor. Exp. (2009) P02005.
[33] K. Nho and E. Manousakis, Phys. Rev. B **68**, 174503 (2003).
[34] M. E. J. Newman, G. T. Barkema, *Monte Carlo Methods in Statistical Physics* (Oxford University Press, USA, 1999).
[35] U. Wolff, Phys. Rev. Lett. **62**, 361 (1989).
[36] M. Creutz, Phys. Rev. D **36**, 515 (1987).
[37] S. G. Pawig and K. Pinn, Int. J. Mod. Phys. C **09**, 727 (1998).
[38] W. H. Press, S. A. Teukolsky, W. T. Vetterling, and B. P. Flannery, *Numerical Recipes in Fortran 77: The Art of Scientific Computing*, Vol. 277 (Cambridge University Press, Cambridge, UK, 2001).
[39] A. M. Ferrenberg and R. H. Swendsen, Phys. Rev. Lett. **61**, 2635 (1988).
[40] A. Cuccoli, V. Tognetti, and R. Vaia, Phys. Rev. B **52**, 10221 (1995).
[41] J. M. Kosterlitz, J. Phys. C: Sol. Stat. Phys. **7**, 1046 (1974).
[42] Y. Z. Sun, J. C. Liang, S. L. Xu, and L. Yi, Physica A **389**, 1391 (2010).
[43] G. M. Wysin, A. R. Pereira, I. A. Marques, S. A. Leonel, and P. Z. Coura, Phys. Rev. B **72**, 094418 (2005).
[44] Y.-Z. Sun, L. Yi, and G. M. Wysin, Phys. Rev. B **78**, 155409 (2008).
[45] Y. Z. Sun, L. Yi, and Y. H. Gao, Sol. Stat. Commun. **149**, 1000 (2009).
[46] H. G. Evertz and D. P. Landau, Phys. Rev. B **54**, 12302 (1996).
[47] M. E. Fisher, M. N. Barber, and D. Jasnow, Phys. Rev. A **8**, 1111 (1973).
[48] A. Garg, R. Pandit, S. A. Solla, and C. Ebner, Phys. Rev. B **30**, 106 (1984).
[49] Y. H. Li and S. Teitel, Phys. Rev. B **40**, 9122 (1989).
[50] P. Olsson, Phys. Rev. B **52**, 4526 (1995).
[51] L. M. Castro, A. S. T. Pires, and J. A. Plascak, J. Mag. Mag. Mat. **248**, 62 (2002).
[52] M. Campostrini, M. Hasenbusch, A. Pelissetto, and E. Vicari, Phys. Rev. B **74**, 144506 (2006).
[53] J. B. Santos-Filho and J. A. Plascak, Comput. Phys. Commun. **182**, 1130 (2011).